Component-Controllable $WS_{2(1-x)}Se_{2x}$ Nanotubes for Efficient Hydrogen Evolution Reaction

Kai Xu,[§] Fengmei Wang,[§] Zhenxing Wang, Xueying Zhan, Qisheng Wang, Zhongzhou Cheng, Muhammad Safdar, and Jun He*

National Center for Nanoscience and Technology, Beijing 100190, People's Republic of China. [§]K. Xu and F. Wang contributed equally to this work.

ABSTRACT Owing to the excellent potential for fundamental research and technical applications in optoelectronic devices and catalytic activity for hydrogen evolution reaction (HER), transition metal dichalcogenides have recently attracted much attention. Transition metal sulfide nanostructures have been reported and demonstrated promising application in transistors and photodetectors. However, the growth of transition metal selenide nanostructures and their applications has still been a challenge. In this work, we successfully synthesized high-quality WSe_2 nanotubes on carbon fibers *via* selenization. More importantly, through optimizing the growth conditions, ternary $WS_{2(1-x)}Se_{2x}$ nanotubes were synthesized and the composition of S and Se can be systematically controlled. The as-grown $WS_{2(1-x)}Se_{2x}$ nanotubes on carbon fibers, assembled as a working electrode, revealing low overpotential, high exchange current density, and small series resistance, exhibit excellent electrocatalytic properties for hydrogen evolution reaction. Our study provides the experimental groundwork for the synthesis of low-dimensional transition metal dichalcogenides and may open up exciting opportunities for their application in electronics, photoelectronics, and catalytic electrochemical reactions.

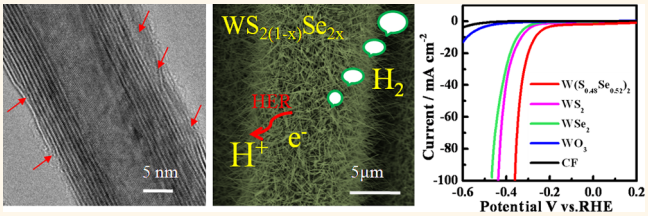

KEYWORDS: WSe_2 nanotube · $WS_{2(1-x)}Se_{2x}$ nanotube · chemical vapor deposition · carbon fiber · hydrogen evolution reaction

With strong in-plane bonding and weak out-of-plane van der Waals interactions between individual sandwiched X−M−X layers, transition metal dichalcogenides (TMDs) have attracted enormous attention not only for fundamental research but also for novel material engineering.[1−10] One-dimensional TMD materials, such as nanotubes (NTs), nanowires (NWs), and nanoribbons (NRs), could not only provide a model system for investigating the dependence of mechanical, thermal, and electronic transport and optical properties on dimensional confinement but also play an important role as active components in fabricating nanoscale electronic and photoelectronic devices.[11−13] Meanwhile, one-dimensional TMD materials are also catalytically active for many important electrochemical reactions such as hydrogen evolution reaction (HER) and oxygen reduction reaction.[14−17]

Low-dimensional TMD materials, such as WS_2 and WSe_2, display enormous advantages and potential prospects for nanostructure devices and applications. For example, WS_2 NTs have recently been synthesized *via* a fluidized bed reactor and a gas-phase reaction.[18−20] High-performance photodetectors based on WS_2 NTs exhibited short rise and decay times of a few hundred microseconds, a high on/off ratio of 336, and an external quantum efficiency of 615%.[21] Field-effect transistors based on individual WS_2 NTs demonstrated a high field-effect mobility of up to 50 $cm^2 V^{-1} s^{-1}$, a free charge carrier density of 10^{19} cm^{-3}, and an unexpectedly high current-carrying capacity of over 0.6 mA.[11] WSe_2 has been found to be the first TMD material combining p-type and n-type behaviors in the same material. However, previous research on WSe_2 is largely based on thin films.[22] For instance, p-type WSe_2 nanosheet field-effect transistors demonstrate a high effective hole mobility of 250 $cm^2 V^{-1} s^{-1}$, perfect subthreshold swing of 60 mV/dec, and I_{ON}/I_{OFF} of $>10^6$ at room temperature.[23] Meanwhile, n-type WSe_2 nanosheet field-effect transistors reveal an electron mobility of 142 $cm^2 V^{-1} s^{-1}$ and a record ON-current of 210 $\mu A/\mu m$.[24] To date, few studies have been reported on the application of one-dimensional WSe_2, such

* Address correspondence to hej@nanoctr.cn.

Received for review June 3, 2014 and accepted August 11, 2014.

Published online August 11, 2014
10.1021/nn503027k

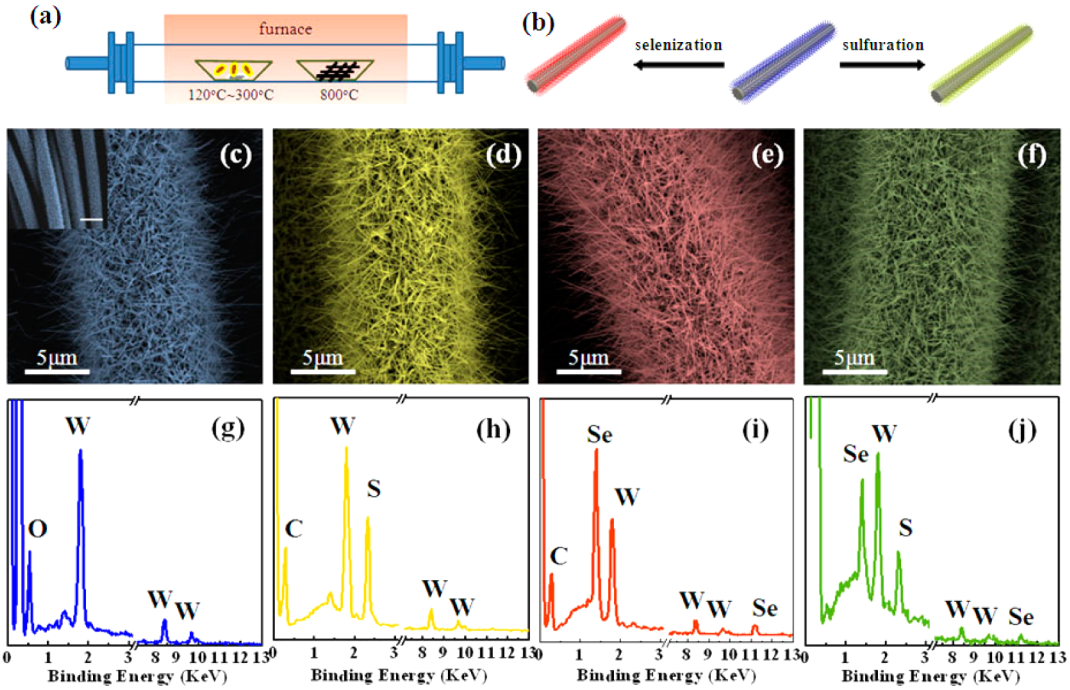

Figure 1. (a) Schematic diagram of the experimental setup of the fabrication of WO_3 NWs and WS_2, WSe_2, and $WS_{2(1-x)}Se_{2x}$ NTs. (b) Schematic diagram of WO_3 NWs converting to WS_2 and WSe_2 NTs on carbon fibers by sulfuration and selenization. Magnified SEM of (c) WO_3 NWs and (d) WS_2, (e) WSe_2, and (f) $WS_{2(1-x)}Se_{2x}$ NTs. EDS pattern of (g) WO_3 NWs and (h) WS_2, (i) WSe_2, and (j) $WS_{2(1-x)}Se_{2x}$ NTs.

as NWs or NTs. This is likely due to the great challenge of synthesizing WSe_2 NWs or NTs.

Motivated by the success in WS_2 NTs, chemical vapor deposition (CVD) is chosen in our attempt to synthesize WSe_2 NTs. Furthermore, the growth of high-quality $WS_{2(1-x)}Se_{2x}$ NT is proposed, and the control of S and Se components provides an effectual approach to modify its physical and chemical properties. Among various substrates for CVD synthesis,[25−27] carbon fibers (CFs), used as a flexible substrate, provide more space for the growth than other rigid substrates. Meanwhile, CFs present outstanding tensile properties, wonderful electric conductivity, and high thermal and chemical stabilities. More importantly, they are low-cost, lightweight, flexible, recyclable, and environmentally friendly. Synthesizing one-dimensional TMD NTs on CFs not only makes use of the merits of CFs but also extremely enhances and deepens the potential advantage of one-dimensional TMD NTs in catalytic reactions, energy storage, and so forth.

Herein, we present the design and fabrication of high-quality WS_2, WSe_2, and their component-controllable $WS_{2(1-x)}Se_{2x}$ NTs on flexible CFs *via* a chemical vapor method. WS_2 and WSe_2 NTs were controllably synthesized by transforming WO_3 NWs on CFs with sulfur and selenium power as precursors. The selenium concentration of $WS_{2(1-x)}Se_{2x}$ NTs can be systematically controlled by adjusting the growth conditions. WS_2, WSe_2, and $WS_{2(1-x)}Se_{2x}$ NTs synthesized on CFs served as working electrodes in the three-electrode system, displaying low overpotential, high exchange current density, and small series resistance and Tafel slope, suggesting the excellent electrocatalytic properties of TMD NTs for HER.

RESULTS AND DISCUSSION

Figure 1a schematically illustrates our experimental setup for the growth of WO_3 NWs and WS_2, WSe_2, and their ternary $WS_{2(1-x)}Se_{2x}$ NTs in a horizontal two-zone tube furnace. Figure 1c−f shows typical morphology images of WO_3 NWs and WS_2, WSe_2, and $WS_{2(1-x)}Se_{2x}$ ($x = 0.52$) NTs grown on highly flexible CFs. The entire surfaces of the CFs are covered vertically and uniformally with high-density WO_3 NWs, as shown in Figure 1c. The diameter and length of typical WO_3 NWs were found to be ~100 nm and ~5 μm, respectively. Through sulfuration and selenization of the WO_3 NWs, the WS_2 and WSe_2 NTs were synthesized at 800 °C, as manifested in Figure 1d and e. For the synthesis of $WS_{2(1-x)}Se_{2x}$ NTs in Figure 1f, the controllable element component of ternary NTs is successfully achieved by altering the proportion of S and Se precursors. Because of using WO_3 NWs as a conversion template, the diameter and length of the WS_2 and WSe_2 NTs are comparable as those of WO_3 NWs. It is worth pointing out that, for the synthesis of the WS_2 NTs, the sulfuration of the WO_3 NWs is typically performed at 800 °C in an Ar atmosphere. The chemical reaction is described as

$$2WO_3 + 7S \rightarrow 2WS_2 + 3SO_2 \quad (1)$$

However, for the synthesis of the WSe_2 NTs, because the chemical reactivity of Se is lower than that of S, the

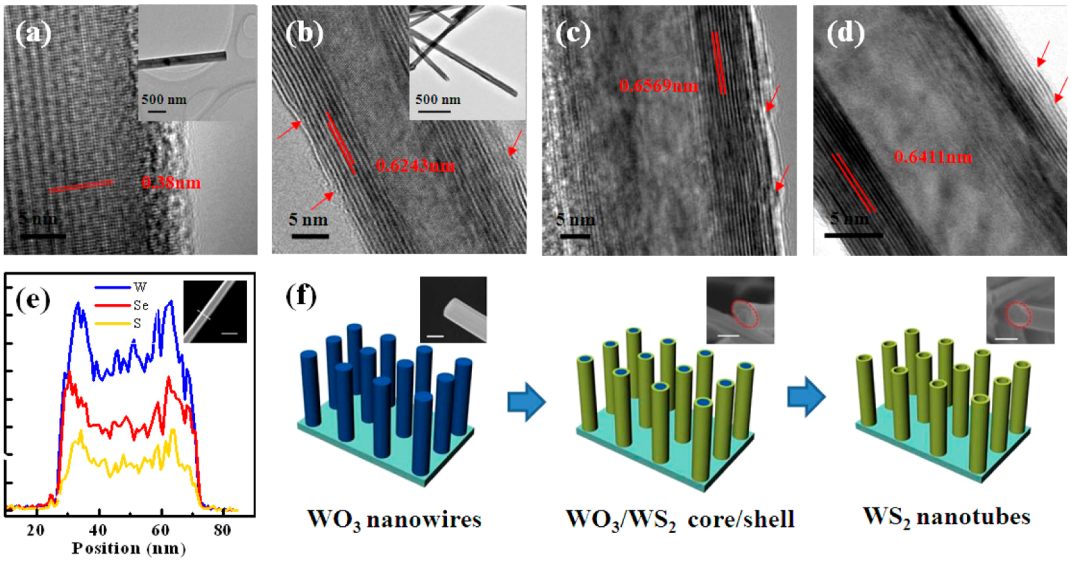

Figure 2. HRTEM image of (a) WO_3 NWs and (b) WS_2, (c) WSe_2, and (d) $WS_{2(1-x)}Se_{2x}$ NTs. Red arrows indicate layer dislocations in the walls of NTs. (e) EDS line-scanning reveals the high intensity of W, S, and Se elements on both sides. (f) Growth process of WO_3 NWs converting to WS_2, WSe_2, and $WS_{2(1-x)}Se_{2x}$ NTs on CFs by sulfuration and selenization.

selenization condition of WO_3 NWs should be changed compared with the sulfuration condition by increasing the temperature of the precursors to enhance the chemical reactivity.[28] The formation is characterized by the following chemical reaction:

$$2WO_3 + 7Se \rightarrow 2WSe_2 + 3SeO_2 \qquad (2)$$

X-ray energy dispersive spectroscopy (EDS) analysis was also conducted to confirm the synthesis of WO_3 NWs and WS_2, WSe_2, and $WS_{2(1-x)}Se_{2x}$ NTs. The corresponding EDS characterization in Figure 1g−j confirmed the existence of the elements W, O, S, and Se. As displayed in Figure 1h and i, the atomic percent of W, S, or Se is exactly 1:2, and the EDS spectrum (Figure 1j) demonstrates that the $WS_{2(1-x)}Se_{2x}$ NTs consist of W, S, and Se elements (the C signal comes from CFs), with the Se mole fraction (x = Se/(S + Se)) of 0.52, indicating the composition of the NT as $WS_{2(0.48)}Se_{2(0.52)}$. Furthermore, EDS mapping analysis of elements W, S, and Se in Figure S1 from a select area of a single $WS_{2(1-x)}Se_{2x}$ NT confirms the alloy $WS_{2(1-x)}Se_{2x}$ structure.

Figure 2a−d shows the transmission electron microscopy (TEM) image of WO_3 NWs and WS_2, WSe_2, and $WS_{2(1-x)}Se_{2x}$ (x = 0.52) NTs. The lattice fringe with distance of 0.38 nm was obtained in Figure 2a, corresponding to the (002) plane of monoclinic WO_3. The crystal structure of WS_2, WSe_2, and $WS_{2(1-x)}Se_{2x}$ (x = 0.52) NTs was confirmed by the lattice image, clearly suggesting the morphology of multiwall nanotubes. Generally, the synthetic WS_2, WSe_2, and $WS_{2(1-x)}Se_{2x}$ (x = 0.52) NTs display full openings, but for some WS_2 NTs, the opening seems to be sealed when the growth is terminated in Figure S2a. The spacing of WS_2, WSe_2, and $WS_{2(1-x)}Se_{2x}$ (x = 0.52) NTs between lattice fringes is respectively 0.6243, 0.6569, and 0.6411 nm, corresponding to previously reported values.[18,29,30] Scanning transmission electron microscopy (STEM) was conducted for $WS_{2(1-x)}Se_{2x}$ NTs, shown in Figure 2e. EDS line scanning (indicated by a line in Figure 2e inset) and the mapping (Figure S3) of W, S, and Se across the $WS_{2(1-x)}Se_{2x}$ NTs could better illustrate the nanotube configuration clearly: the profile of three elements showed higher intensity on both sides. On the basis of the present measurements and the proposed model,[19,31−33] we can visualize the growth process of WS_2 NTs in Figure 2f. At the first stage of the reaction, the S atoms in the tube furnace rapidly exchange with surface oxygen atoms of WO_3, forming a closed WS_2 shell, which encapsulates the entire WO_3 NWs. This stage of shell synthesis is very fast, lasting only a few seconds.[19,33] The WS_2 shell usually contains several WS_2 layers, and once the outer WS_2 layers developed, the sulfuration reaction slows down since the passivation of the outer WS_2 layers prohibits direct contact between S atoms and WO_3 NWs. The second stage of the reaction is a slow process of sulfuration of the WO_3 NW core, which depends on the diffusion of S atoms *via* a WS_2 shell. However, S atoms hardly diffuse through the perfectly crystalline WS_2 layers due to their large diameter. Hopping through defects in the WS_2 layers allows S atoms to go inside. Once the S atoms hop into an inner layer, they diffuse between the two WS_2 layers rapidly until the S atoms encounter another defect in the inner WS_2 layer and another hopping occurs, and so forth. The probability of hopping is rather low, and this stage may take tens of minutes to several hours, which depends on the size of the NWs and the reaction temperature. Eventually, the S atoms thread through outer WS_2 layers and react with the WO_3 core completely. In this stage, WO_3 is partially reduced by S vapor to form suboxide species WO_{3-x},

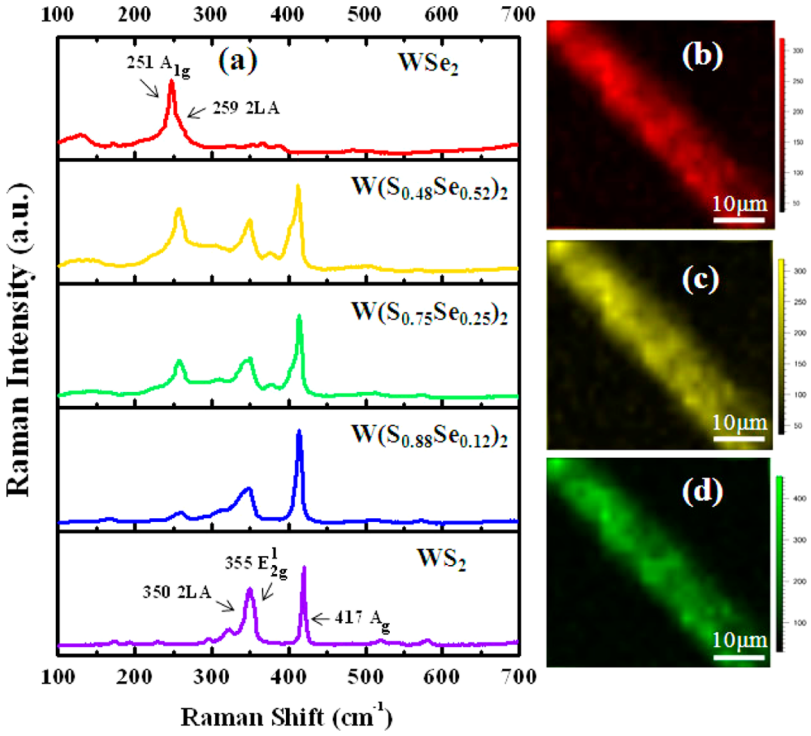

Figure 3. (a) Raman spectra of WS_2, WSe_2, and $WS_{2(1-x)}Se_{2x}$ (x = 0.12, 0.25, and 0.52) NTs. Raman intensity mapping for (b) the A_{1g} mode of WSe_2 NTs and the (c) E^1_{2g} and (d) A_{1g} modes of WS_2 NTs.

which is further sulfurized to WS_2.[34] The synthesis mechanism of WSe_2 NTs is similar to that of WS_2 NTs. To ensure the reaction of S and Se powder with WO_3 simultaneously, it is necessary to rapidly increase the source temperature due to the difference of sublimation temperatures of S and Se. Increasing the temperature quickly to high temperature may lead to a violent reaction, leading to increased defects and exposed edge sites in ternary $WS_{2(1-x)}Se_{2x}$ NTs. As we know that WS_2, WSe_2, and $WS_{2(1-x)}Se_{2x}$ are intrinsically layered structures, reaction with the superficial WO_3 starts isotropically when WO_3 NWs are situated in a S or Se atmosphere. Then S or Se vapor threads through the outer layers and reacts with the WO_3 core isotropically. Thus, WS_2 and WSe_2 appear layer by layer, and WS_2 and WSe_2 NTs are eventually grown. Compared with NWs, NTs show a larger specific surface area due to their hollow structure. Moreover, the HRTEM images present the layer dislocations and defects indicated by red arrows in the walls in Figure 2b–d. As shown in Figure S2c, some small disordered nanodomains emerging from the wall of the nanotube suggest that our NTs are not flawless. From the TEM and HRTEM of $WS_{2(1-x)}Se_{2x}$ NTs in Figure S3, the NTs possess defective walls, marked in red color (Figure S3c), and rough edges. Therefore, the layered and hollow structure of WS_2, WSe_2, and $WS_{2(1-x)}Se_{2x}$ NTs can make them superior with respect to some important practical applications.

Raman spectra for WS_2, WSe_2, and $WS_{2(1-x)}Se_{2x}$ NTs excited by a unpolarized 532 nm laser in backscattering geometry are shown in Figure 3. For the synthesized WS_2 NTs, the Raman spectrum includes three first-order modes: LA (M) at 176 cm^{-1}, E^1_{2g} (Γ) at 355 cm^{-1}, and A_{1g} (Γ) at 417 cm^{-1}, as shown in Figure 3a. Most of the additional peaks belong to a multiphonon combination of three modes.[35] For example, the bands at 230 and 296 cm^{-1}, attributed to A_{1g} (Γ)−LA (M) and 2LA (M)−$2E^2_{2g}$ (M), are also identified. In contrast, only one prominent peak in WSe_2 NTs is distinctly seen in the region where we expect A_{1g} (Γ) and E^1_{2g} (Γ) peaks. Although the A_{1g} (Γ) mode at 251 cm^{-1} overlaps with the E^1_{2g} (Γ) mode at 248 cm^{-1} and the 2LA (M) mode at 259 cm^{-1}, the multiple-peak Lorentzian fitting presented in Figure S4 clearly separates their individual contributions.[36] For the ternary $WS_{2(1-x)}Se_{2x}$ NTs with different components, we clearly observe the increasing of the E^1_{2g} (Γ) mode at 248 cm^{-1} and the 2LA (M) mode at 259 cm^{-1} with enhancing the content of Se gradually. By Lorentzian fitting of the A_{1g} mode of WS_2 NTs in Figure 3a, the full widths at half-maximum (fwhm) of $WS_{2(1-x)}Se_{2x}$ NTs (x = 0, 0.12, 0.25, 0.52) are 4.79, 8.182, 8.441, and 10.261 cm^{-1}. Thus, the $WS_{2(1-x)}Se_{2x}$ NTs with more elemental disorders show much more peak broadening. Raman mapping of the ternary $WS_{2(1-x)}Se_{2x}$ NTs (x = 0.52) provides the spatial intensity maps of the 2LA (M), E^1_{2g} (Γ), and A_{1g} (Γ) mode in Figure 3b–d, demonstrating the uniformity of our samples.

X-ray photoemission spectroscopy (XPS) was acquired to measure the binding energies of W, S, and Se in our WS_2, WSe_2, and $WS_{2(1-x)}Se_{2x}$ NTs, as shown in Figure 4. The binding energies of W $4f_{7/2}$ and W $4f_{5/2}$ slightly shift from 33.2 and 35.4 eV in WS_2 NTs to

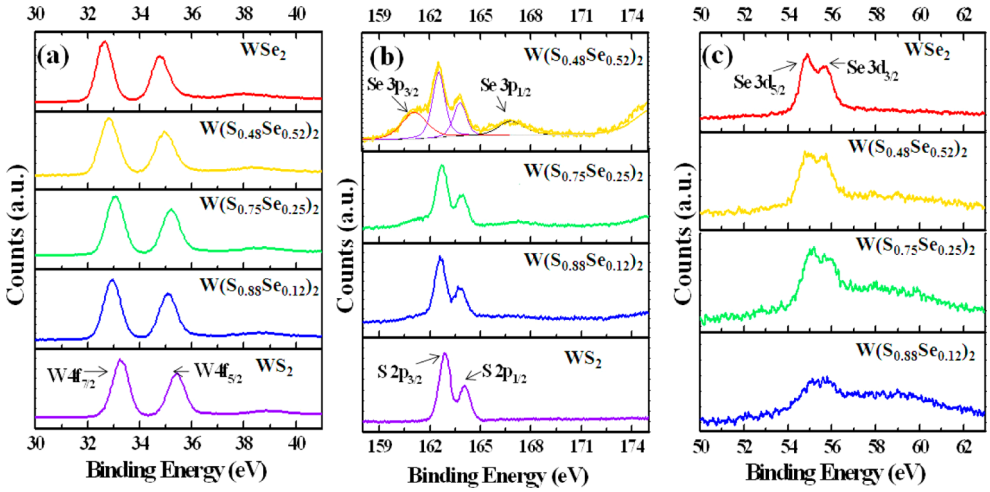

Figure 4. (a–c) XPS spectra of WS_2, WSe_2, and $WS_{2(1-x)}Se_{2x}$ ($x = 0.12$, 0.25, and 0.52) NTs, where the (a) W $4f_{7/2}$ and W $4f_{5/2}$, (b) S $2p_{3/2}$ and S $2p_{1/2}$, and (c) Se $3d_{5/2}$ and Se $3d_{3/2}$ were identified. Note that Se $3p_{3/2}$ (161 eV) and Se $3p_{1/2}$ (166.8 eV) appear and become dominant with increasing Se content in the $WS_{2(1-x)}Se_{2x}$ NTs.

32.6 and 34.7 eV in WSe_2 NTs in Figure 4a, in agreement with previously reported values for the WS_2 and WSe_2 systems.[37,38] The weak peak at 37.8 eV corresponds to W $4f_{5/2}$ from WO_3 due to the oxidation during sample preparation. The peaks at 162.8 and 164 eV are attributed to S $2p_{3/2}$ and S $2p_{1/2}$ binding energies, respectively, as shown in Figure 4b.[37] Note that with increasing Se concentration from 0 to 52%, the peaks of Se $3p_{3/2}$ (161 eV) and Se $3p_{1/2}$ (166.8 eV) appear and become dominant.[39] Se $3d_{5/2}$ and Se $3d_{3/2}$, located at 54.8 and 55.7 eV, exhibit around the same peak positions for WSe_2 and $WS_{2(1-x)}Se_{2x}$ NTs, as shown in Figure 4c. Meanwhile, the more accurate stoichiometric atom ratio of W:S and W:Se from XPS analysis is ~1:2.1 and 1:2.2, showing a higher ratio. On the basis of the growth mechanism above, S or Se atoms diffuse through outer layers and react quickly with the WO_3 core. At the end of the reaction, S or Se residue may reside in the NTs, leading to a little higher S or Se ratio.

Presently, new electrocatalysts based on TMDs, such as MoS_2 and $MoSe_2$, for hydrogen evolution reaction have been researched to replace platinum. Much of the experimental work has suggested that the exposed edge sites and conductivity of TMDs are indispensable for excellent HER performance.[15,39,41] WS_2 nanosheets and WSe_2 nanofilm also demonstrated excellent HER properties in some reported works.[16,38] Inspired by the research results, we believe that our WS_2, WSe_2, and $WS_{2(1-x)}Se_{2x}$ NTs may possess excellent HER properties due to increased surface area of multilayered NTs on rough and curved CFs. Moreover, as suggested in Figure 2, Figure S2 and Figure S3 of the HRTEM images of WS_2, WSe_2, and $WS_{2(1-x)}Se_{2x}$ NTs, layer dislocations and defects existing on the NTs' walls enhance the exposed edge sites. The disordered nanodomains on the walls of the samples can act as active sites for HER performance. On the basis of the aforementioned analysis, electrochemical measurements with the various NTs as the catalysts were carried out. The polarization curves after *iR* correction obtained at the voltage sweeping rate of 2 mV/s reveal the normalized current density *vs* voltage (*vs* RHE) of all samples in Figure 5a. Compared with WO_3 NWs and pure CFs, all NTs on CFs display a small onset overpotential, above which the cathodic current increases rapidly under more negative potentials.[16] The large electroactive surface area and the dislocations obtained during the sulfuration and selenization process may lead to good catalytic activity of the products.[15] The unique arrangement of nanodomains shown in Figure S2c can partially retain the 2D electron conjugation along the walls of the NTs, leading to fast interdomain electron transport. The electrocatalytic property of our WSe_2 NTs on CFs is comparable with that of WS_2 NTs, suggesting the capability of WSe_2 NTs for HER. Even more impressively, the $WS_{2(1-x)}Se_{2x}$ NT ($x = 0.52$) electrode shows the best HER catalytic activity among all NT electrocatalysts. Some research works have reported that different elemental incorporation can realize a synergistic effect of both rich active sites and good conductivity of the electrocatalyst.[40] In this work, during the simultaneous sulfuration and selenization process of WO_3 NWs on CFs, the ternary $WS_{2(1-x)}Se_{2x}$ NTs provide both increased number of active sites and higher conductivity for HER performance. Figure S3 reveals the increased defects and exposed edge sites in the composition of ternary $WS_{2(1-x)}Se_{2x}$ NTs on CFs. The synergistic effect of increased active sites and excellent conductivity of $WS_{2(1-x)}Se_{2x}$ NTs improves the HER performance. The cathodic current density is proportional to the quality of evolved hydrogen. Therefore, the large current density at the same potential here indicates prominent hydrogen evolution behavior and good charge transfer from the film to the electrode. Tafel plots in Figure 5b were obtained for further insight into the electrocatalytic activity of all the electrodes.[40,41]

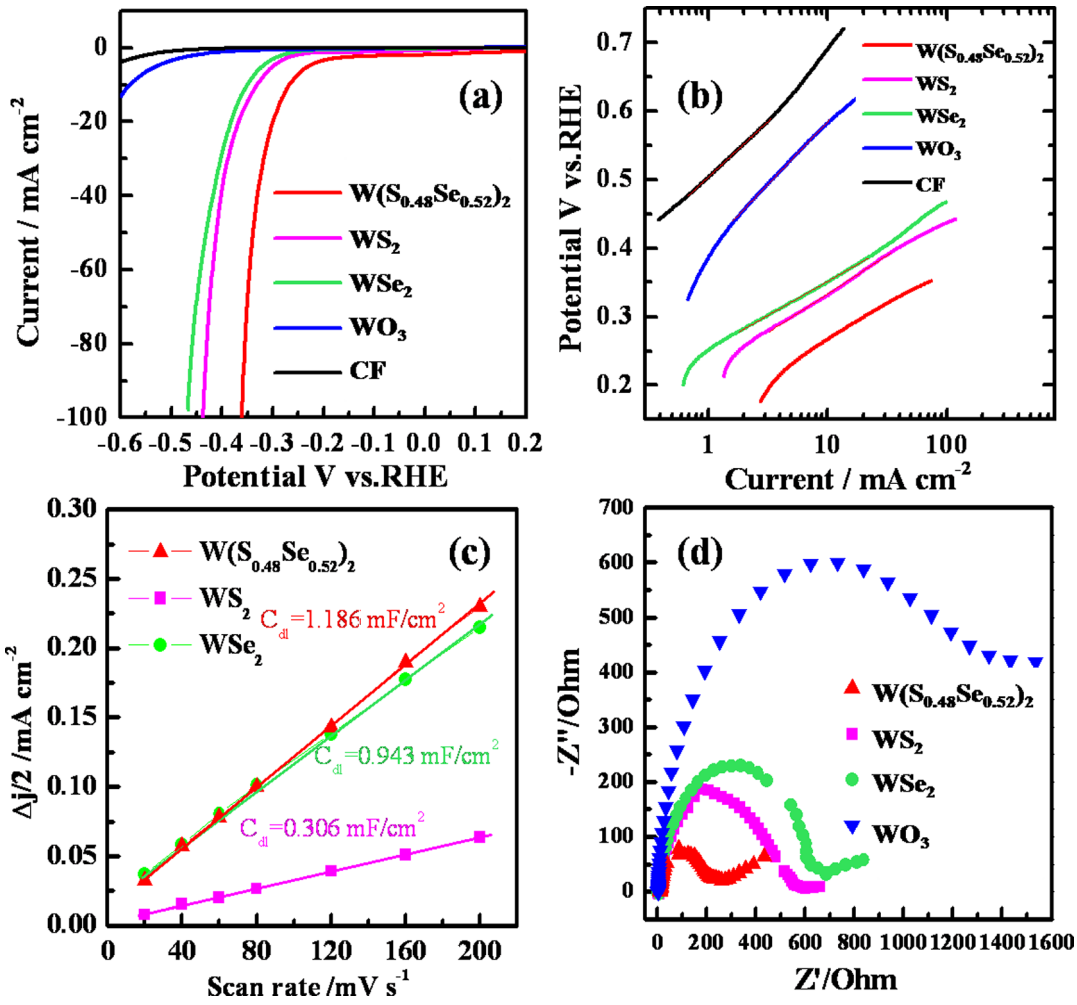

Figure 5. HER electrocatalytic properties of WO_3 NWs, WS_2 NTs, WSe_2 NTs, and $WS_{2(1-x)}Se_{2x}$ NTs. (a) Polarization curves (after *iR* correction) of WO_3 NWs and WS_2, WSe_2, and $WS_{2(1-x)}Se_{2x}$ ($x = 0.52$) NTs on CFs along with that corresponding to pure CFs for comparison. (b) Corresponding Tafel plots obtained from the polarization curves of pure CFs, WO_3 NWs, and WS_2, WSe_2, and $WS_{2(1-x)}Se_{2x}$ ($x = 0.52$) NTs on CFs. (c) Liner fitting of the capacitive currents of the catalysts *vs* scan rate. The calculated double-layer capacitances are 1.186, 0.943, and 0.306 mF for $WS_{2(1-x)}Se_{2x}$, WSe_2, and WS_2 NTs, respectively. (d) Nyquist plots of different samples showing the facile electrode kinetics.

The WSe_2 and $WS_{2(1-x)}Se_{2x}$ NTs electrodes display lower Tafel slopes of 0.099 and 0.105 V per decade than that of the WS_2 NT electrode (~0.113 V per decade), which is comparable with that of published WS_2 NTs (~0.109 V per decade).[42] A small Tafel slope will be beneficial in practical applications, because it will result in a strongly enhanced HER rate at a moderate increase of overpotential.[43,44] Meanwhile, as an important parameter describing HER activity of a catalyst, the exchange current densities of WS_2, WSe_2, and $WS_{2(1-x)}Se_{2x}$ NTs are determined to be 0.012, 0.003, and 0.029 mA cm^{-2} by fitting the linear portion of the Tafel plot at low cathodic current to the Tafel equation. The $WS_{2(1-x)}Se_{2x}$ NTs show remarkable exchange current density, which is the largest value among all NT electrodes and about 5 times larger than the value obtained from the WO_3 NW electrode (0.006 mA cm^{-2}). The lowest overpotential and largest exchange current density of $WS_{2(1-x)}Se_{2x}$ NTs on CFs demonstrate the superior HER activity and potential applications. The surface curvature and roughness of the carbon fiber substrate are likely responsible for the high exchange current density of the NTs and maximize the exposed edge sites.[38] Significantly, this result also proves that the synergistic effect of increased active sites and excellent conductivity of $WS_{2(1-x)}Se_{2x}$ NTs makes a contribution to the better HER performance than that of WS_2 and WSe_2 NTs.

To estimate the differences in electrochemically active surface areas of various catalysts, the cyclic voltammetry (CV) method was employed to measure the electrochemical double-layer capacitance (EDLC), C_{dl}.[14,40] The potential range where no faradic current was observed was selected for accurate measurements of the large active surface area of the electrode (Figure S5). Cyclic voltammetry curves were obtained at various scan rates (20, 40, 60, *etc.* mV s^{-1}) at 0.12−0.22 V *vs* the RHE region. The halves of the positive and negative current density differences at the center of the scanning potential ranges are plotted *vs* the voltage scan

rate in Figure 5c.[14,45] The C_{dl} of the various electrodes can be calculated to be 1.186, 0.943, and 0.306 mF/cm^2 for $WS_{2(1-x)}Se_{2x}$, WSe_2, and WS_2 NTs, demonstrating that the active area of $WS_{2(1-x)}Se_{2x}$ NTs is about 4 times as large as that of WS_2 NTs. This result confirms that the $WS_{2(1-x)}Se_{2x}$ NT electrode possesses the largest active surface area among all electrodes. The largest electrochemically active area indicates the proliferation of the active sites and exposed edges on the walls of the $WS_{2(1-x)}Se_{2x}$ NTs, determining the superior HER activity. Besides the edge sites, the conductivity of these catalysts is also essential for excellent HER performance. To understand clearly the electrical properties of the as-prepared electrodes/solution interfaces, electrochemical impedance spectroscopy (EIS) is performed to investigate the electrode kinetics of the HER process. As shown in Figure 5d, the Nyquist plots reveal that the charge-transfer resistance (R_{ct}) of WS_2, WSe_2, and $WS_{2(1-x)}Se_{2x}$ NTs are approximately 565, 624, and 204 Ω, respectively. The ternary $WS_{2(1-x)}Se_{2x}$ NTs possess the lowest R_{ct}, and they are an excellent catalyst for HER. The small series resistance of ~5 Ω observed for all samples ensures the importance of the direct synthesis on a conductive substrate, which enables simple and effective electrical integration that minimizes parasitic ohmic losses. The results confirm that sulfuration and selenization are effective methods to obtain electrocatalysts of WS_2, WSe_2, and ternary $WS_{2(1-x)}Se_{2x}$ NTs from WO_3 NWs in an *in situ* process. The strong bonding between the nanotubes and substrate confirms that our samples can directly be used in diverse water electrolysis devices as low-cost, high-performance, and stable HER catalysts. As displayed in Figure S5a, a continuous HER process occurred at a constant overpotential (0.298 V *vs* RHE). The as-measured time-dependent curves after ~2 h testing reveal relatively stable corresponding current densities of these electrodes, which suggests their excellent electrochemical stabilities under HER conditions. The degradation of current densities of WS_2, WSe_2, and $WS_{2(1-x)}Se_{2x}$ NTs after a long period of ~2 h might be caused by the consumption of H^+ or the accumulation of H_2 bubbles on the electrode surface. Moreover, the good chemical stability of $WS_{2(1-x)}Se_{2x}$ NTs is also demonstrated in Figure S6b, indicating that only a slight change in HER activity occurs even after 3 months of storage under an air atmosphere.

CONCLUSION

In summary, we have synthesized WS_2, WSe_2, and their component-controllable $WS_{2(1-x)}Se_{2x}$ NTs grown on highly flexible CFs. These high-quality NTs were synthesized at 800 °C with 50 sccm Ar gas for 30−60 min. More importantly, the Se composition of ternary $WS_{2(1-x)}Se_{2x}$ NTs could be controlled by adjusting the proportions of S and Se precursors. Combining SEM and TEM measurements, we find the diameter and length of WS_2, WSe_2, and $WS_{2(1-x)}Se_{2x}$ NTs are mainly ~100 nm and ~5 μm, respectively. Due to WO_3 NWs as a conversion template, the diameter and length of the WS_2, WSe_2, and $WS_{2(1-x)}Se_{2x}$ NTs are comparable to those of WO_3 NWs. The crystal structure and configuration of WS_2, WSe_2, and $WS_{2(1-x)}Se_{2x}$ NTs were clearly characterized by HRTEM and the uniformity was characterized by Raman mapping. XPS measurements reveal the binding energies of W, S, and Se, corresponding to reported values for the WS_2 and WSe_2 systems. Our CVD WS_2, WSe_2, and $WS_{2(1-x)}Se_{2x}$ NTs on CFs served as working electrodes for HER, exhibiting outstanding electrocatalytic properties. The ternary $WS_{2(1-x)}Se_{2x}$ NTs provide both increased number of active sites and higher conductivity for excellent HER performance. Our research on the fabrication and application of WS_2, WSe_2, and $WS_{2(1-x)}Se_{2x}$ NTs has laid a solid foundation for photoelectronic devices and low-cost, efficient, and stable HER electrocatalysts. Even more impressively, scalably synthesized WSe_2 and $WS_{2(1-x)}Se_{2x}$ NTs on CFs will broaden our vision to fabricate electrochemical catalysts and other electronic devices.

EXPERIMENTAL SECTION

Synthesis of WO_3 Nanowires on Carbon Fibers. Prior to the growth, CFs were immersed into a (1:1:1) mixture of acetone, ethanol, and deionized water for ultrasonic cleaning for at least 30 min. The WO_3 NWs were synthesized by a catalyst-free, high-temperature evaporation process. In the typical WO_3 NW synthesis process, WO_3 powder (99% Alfa Aesar) as the source was placed at the center of a tube furnace, and the CFs, as flexible substrate, were located near the WO_3 powder, downstream by 8−12 cm. Before increasing the temperature, the tube was flushed with Ar gas three times and pumped to a vacuum lower than 1 Pa. The furnace temperature was increased to 800−1000 °C at a heating rate of 30 °C min^{-1} and kept for 40−60 min under 100 sccm Ar gas flow. After the synthesis process, the furnace was allowed to cool to room temperature.

Synthesis of WS_2, WSe_2, and $WS_{2(1-x)}Se_{2x}$ Nanotubes on Carbon Fibers. The CFs with largely WO_3 NWs were placed in the back zone, while S or Se powder (~0.4 g, 99.8% Alfa Aesar) as precursor was located in the front zone, as shown in Figure 1a. When the back zone was raised to 800 °C at a heating rate of 20 °C min^{-1}, the front zone began to increase in temperature to 130−150 °C or 280−320 °C at a rate of 10 °C min^{-1}. The conversion process was maintained for 30−60 min with 50 sccm Ar gas. After the conversion process, the furnace was allowed to cool to room temperature. For the synthesis of $WS_{2(1-x)}Se_{2x}$ NTs, S and Se powders were mixed and ground in different proportions. When the back zone reached 800 °C, it was necessary to rapidly increase the front zone to 280−320 °C at a rate of 60−100 °C min^{-1}. Finally, the mass loading of the grown NTs on CFs is about 0.21 mg/cm^2, determined by using an electronic balance (BT 125D) with ±10 μg accuracy.

Material Characterization and Electrochemical Measurement. The morphologies and microstructures of WO_3 NWs and WS_2, WSe_2, and $WS_{2(1-x)}Se_{2x}$ NTs were characterized by field emission scanning electron microscopy (FESEM, Hitach S-4800)

and by transmission electron microscopy (Tecnai F20). The Raman scattering of WS_2, WSe_2, and $WS_{2(1-x)}Se_{2x}$ NTs was performed on a confocal microscope-based Raman spectrometer (Renishaw InVia, 532 nm excitation laser). Chemical configurations were obtained by X-ray photoelectron spectroscopy (ESCALAB250Xi). Electrochemical measurements were performed in a three-electrode system at an electrochemical station (CHI 660D). All the potentials were calibrated to a reversible hydrogen electrode (RHE). Typically, a piece of CF with NTs served as a working electrode using a Ag/AgCl electrode as the reference electrode and a platinum wire as the counter electrode. Electrochemically inert tape was used to define the 0.75 cm^2 electrode area. Linear sweep voltammetry beginning at 0.2 V and ending at −0.8 V *vs* RHE with a scan rate of 2 mV/s was conducted in 20 mL of a 1 M H_2SO_4 solution. Electrochemical impedance spectroscopy was performed when the working electrode was biased at a constant 0.128 V *vs* RHE while sweeping the frequency from 1 MHz to 0.001 Hz with a 10 mV ac dither. Cyclic voltammograms taken with various scan rates (20, 40, 60, *etc.* mV/s) used to estimate the double-layer capacitance were collected in the 0.12−0.22 V *vs* RHE region.

Conflict of Interest: The authors declare no competing financial interest.

Supporting Information Available: HRTEM and EDS mapping images of elements W, S, and Se. Lorentzian fitting for the WSe_2 multiple peaks at about 250 cm^{-1}. Cyclic voltammetry curves and potentiostatic electrolysis of WS_2, WSe_2, and $WS_{2(1-x)}Se_{2x}$ NTs. This material is available free of charge *via* the Internet at http://pubs.acs.org.

Acknowledgment. This work at the National Center for Nanoscience and Technology was supported by the 973 Program of the Ministry of Science and Technology of China (No. 2012CB934103), the 100-Talents Program of the Chinese Academy of Sciences (No. Y1172911ZX), the National Natural Science Foundation of China (No. 21373065), and Beijing Natural Science Foundation (No. 2144059).

REFERENCES AND NOTES

1. Radisavljevic, B.; Radenovic, A.; Brivio, J.; Giacometti, V.; Kis, A. Single-Layer MoS_2 Transistors. *Nat. Nanotechnol.* **2011**, *6*, 147–150.
2. Lopez-Sanchez, O.; Lembke, D.; Kayci, M.; Radenovic, A.; Kis, A. Ultrasensitive Photodetectors Based on Monolayer MoS_2. *Nat. Nanotechnol.* **2013**, *8*, 497–501.
3. Yin, Z.; Li, H.; Li, H.; Jiang, L.; Shi, Y.; Sun, Y.; Lu, G.; Zhang, Q.; Chen, X.; Zhang, H. Single-Layer MoS_2 Phototransistors. *ACS Nano* **2012**, *6*, 74–80.
4. Splendiani, A.; Sun, L.; Zhang, Y.; Li, T.; Kim, J.; Chim, C. Y.; Galli, G.; Wang, F. Emerging Photoluminescence in Monolayer MoS_2. *Nano Lett.* **2010**, *10*, 1271–1275.
5. Mak, K. F.; Lee, C.; Hone, J.; Shan, J.; Heinz, T. F. Atomically Thin MoS_2: A New Direct-Gap Semiconductor. *Phys. Rev. Lett.* **2010**, *105*, 136805–1−4.
6. Mak, K. F.; He, K.; Shan, J.; Heinz, T. F. Control of Valley Polarization in Monolayer MoS_2 by Optical Helicity. *Nat. Nanotechnol.* **2012**, *7*, 494–498.
7. Lee, H. S.; Min, S. W.; Chang, Y. G.; Park, M. K.; Nam, T.; Kim, H.; Kim, J. H.; Ryu, S.; Im, S. MoS_2 Nanosheet Phototransistors with Thickness-Modulated Optical Energy Gap. *Nano Lett.* **2012**, *12*, 3695–3700.
8. Zhao, W.; Ghorannevis, Z.; Chu, L.; Toh, M.; Kloc, C.; Tan, P. H.; Eda, G. Evolution of Electronic Structure in Atomically Thin Sheets of WS_2 and WSe_2. *ACS Nano* **2012**, *7*, 791–797.
9. Braga, D.; Gutierrez Lezama, I.; Berger, H.; Morpurgo, A. F. Quantitative Determination of the Band Gap of WS_2 with Ambipolar Ionic Liquid-Gated Transistors. *Nano Lett.* **2012**, *12*, 5218–5223.
10. Gutierrez, H. R.; Perea-Lopez, N.; Elias, A. L.; Berkdemir, A.; Wang, B.; Lv, R.; Lopez-Urias, F.; Crespi, V. H.; Terrones, H.; Terrones, M. Extraordinary Room-Temperature Photoluminescence in Triangular WS_2 Monolayers. *Nano Lett.* **2013**, *13*, 3447–3454.
11. Levi, R.; Bitton, O.; Leitus, G.; Tenne, R.; Joselevich, E. Field-Effect Transistors Based on WS_2 Nanotubes with High Current-Carrying Capacity. *Nano Lett.* **2013**, *13*, 3736–3741.
12. Nethravathi, C.; Jeffery, A. A.; Rajamathi, M.; Kawamoto, N.; Tenne, R.; Golberg, D.; Bando, Y. Chemical Unzipping of WS_2 Nanotubes. *ACS Nano* **2013**, *7*, 7311–7317.
13. Ghorbani-Asl, M.; Zibouche, N.; Wahiduzzaman, M.; Oliveira, A. F.; Kuc, A.; Heine, T. Electromechanics in MoS_2 and WS_2: Nanotubes *vs*. Monolayers. *Sci. Rep.* **2013**, *3*, 2961–1−8.
14. Lukowski, M. A.; Daniel, A. S.; Meng, F.; Forticaux, A.; Li, L.; Jin, S. Enhanced Hydrogen Evolution Catalysis from Chemically Exfoliated Metallic MoS_2 Nanosheets. *J. Am. Chem. Soc.* **2013**, *135*, 10274–10277.
15. Xie, J.; Zhang, H.; Li, S.; Wang, R.; Sun, X.; Zhou, M.; Zhou, J.; Lou, X. W.; Xie, Y. Defect-Rich MoS_2 Ultrathin Nanosheets with Additional Active Edge Sites for Enhanced Electrocatalytic Hydrogen Evolution. *Adv. Mater.* **2013**, *25*, 5807–5813.
16. Voiry, D.; Yamaguchi, H.; Li, J.; Silva, R.; Alves, D. C. B.; Fujita, T.; Chen, M.; Asefa, T.; Shenoy, V. B.; Eda, G.; *et al*. Enhanced Catalytic Activity in Strained Chemically Exfoliated WS_2 Nanosheets for Hydrogen Evolution. *Nat. Mater.* **2013**, *12*, 850–855.
17. Perkins, F. K.; Friedman, A. L.; Cobas, E.; Campbell, P. M.; Jernigan, G. G.; Jonker, B. T. Chemical Vapor Sensing with Monolayer MoS_2. *Nano Lett.* **2013**, *13*, 668–673.
18. Zhu, Y. Q.; Hsu, W. K.; Terrones, H.; Grobert, N.; Chang, B. H.; Tenne, M.; Wei, B. Q.; Kroto, H. W.; Walton, D. R. M.; Boothroyd, C. B.; *et al*. Morphology, Structure and Growth of WS_2 Nanotubes. *J. Mater. Chem.* **2000**, *10*, 2570–2577.
19. Margolin, A.; Rosentsveig, R.; Albu-Yaron, A.; Popovitz-Biro, R.; Tenne, R. Study of the Growth Mechanism of WS_2 Nanotubes Produced by a Fluidized Bed Reactor. *J. Mater. Chem.* **2004**, *14*, 617–624.
20. Nath, M.; Govindaraj, A.; Rao, C. N. R. Simple Synthesis of MoS_2 and WS_2 Nanotubes. *Adv. Mater.* **2001**, *13*, 283–286.
21. Zhang, C.; Wang, S.; Yang, L.; Liu, Y.; Xu, T.; Ning, Z.; Zak, A.; Zhang, Z.; Tenne, R.; Chen, Q. High-Performance Photodetectors for Visible and Near-Infrared Lights Based on Individual WS_2 Nanotubes. *Appl. Phys. Lett.* **2012**, *100*, 243101–1−5.
22. Xu, K.; Wang, Z.; Du, X.; Safdar, M.; Jiang, C.; He, J. Atomic-Layer Triangular WSe_2 Sheets: Synthesis and Layer-Dependent Photoluminescence Property. *Nanotechnology* **2013**, *24*, 465705.
23. Fang, H.; Chuang, S.; Chang, T. C.; Takei, K.; Takahashi, T.; Javey, A. High-Performance Single Layered WSe_2 p-FETs with Chemically Doped Contacts. *Nano Lett.* **2012**, *12*, 3788–3792.
24. Liu, W.; Kang, J.; Sarkar, D.; Khatami, Y.; Jena, D.; Banerjee, K. Role of Metal Contacts in Designing High-Performance Monolayer n-Type WSe_2 Field Effect Transistors. *Nano Lett.* **2013**, *13*, 1983–1990.
25. Wang, F.; Wang, Y.; Zhan, X.; Safdar, M.; Gong, J.; He, J. Pt Nanoparticle and CdS Quantum Dot Assisted WO_3 Nanowires Grown on Flexible Carbon Fibers for Efficient Oxygen Production. *CrystEngComm*. **2014**, *16*, 1389–1394.
26. Lu, X.; Zhai, T.; Zhang, X.; Shen, Y.; Yuan, L.; Hu, B.; Gong, L.; Chen, J.; Gao, Y.; Zhou, J.; *et al*. WO_{3-x}@Au@MnO_2 Core-Shell Nanowires on Carbon Fabric for High-Performance Flexible Supercapacitors. *Adv. Mater.* **2012**, *24*, 938–944.
27. Safdar, M.; Wang, Q.; Mirza, M.; Wang, Z.; Xu, K.; He, J. Topological Surface Transport Properties of Single-Crystalline SnTe Nanowire. *Nano Lett.* **2013**, *13*, 5344–5349.
28. Huang, J. K.; Pu, J.; Hsu, C. L.; Chiu, M. H.; Juang, Z. Y.; Chang, Y. H.; Chang, W. H.; Iwasa, Y.; Takenobu, T.; Li, L. J. Large-Area Synthesis of Highly Crystalline WSe_2 Monolayers and Device Applications. *ACS Nano* **2013**, *8*, 923–930.
29. Zhu, Y. Q.; Hsu, W. K.; Grobert, N.; Chang, B. H.; Terrones, M.; Terrones, H.; Kroto, H. W.; Walton, D. R. M.; Wei, B. Q. Production of WS_2 Nanotubes. *Chem. Mater.* **2000**, *12*, 1190–1194.
30. Galván, D. H.; Rangel, R.; Adem, E. WSe_2 Nanotubes: Their Formation by Electron Irradiation. *Fullerene Sci. Technol.* **2000**, *8*, 9–15.

31. Zak, A.; Feldman, Y.; Alperovich, V.; Rosentsveig, R.; Tenne, R. Growth Mechanism of MoS_2 Fullerence-Like Nanoparticles by Gas-Phase Synthesis. *J. Am. Chem. Soc.* **2000**, *122*, 11108–11116.
32. Feldman, Y.; Frey, G. L.; Honyonfer, M.; Lyakhovitskaya, V.; Margulis, L.; Cohen, H.; Hodes, G.; Hutchison, J. L.; Tenne, R. Bulk Synthesis of Inorganic Fullerence-Like MS_2 (M = Mo, W) from the Respective Trioxides and the Reaction Mechanism. *J. Am. Chem. Soc.* **1996**, *118*, 5362–5367.
33. Therese, H. A.; Zink, N.; Kolb, U.; Tremel, W. Synthesis of MoO_3 Nanostructures and their Facile Conversion to MoS_2 Fullerenes and Nanotubes. *Solid State Sci.* **2006**, *8*, 1133–1137.
34. Zhang, Y.; Ji, Q.; Han, G.; Ju, J.; Shi, J.; Ma, D.; Sun, Y.; Zhang, Y.; Li, M.; Lang, X.; *et al*. Dendritic, Transferable, Strictly Monolayer MoS_2 Flake Synthesized on $SrTiO_3$ Single Crystals for Efficient Electrocatalytic Applications. *ACS Nano* **2014**, 10.1021/nn503412w.
35. Berkdemir, A.; Gutierrez, H. R.; Botello-Mendez, A. R.; Perea-Lopez, N.; Elias, A. L.; Chia, C. I.; Wang, B.; Crespi, V. H.; Lopez-Urias, F.; Charlier, J. C.; *et al*. Identification of Individual and Few Layers of WS_2 Using Raman Spectroscopy. *Sci. Rep.* **2013**, *3*, 1755–1−8.
36. Zhao, W.; Ghorannevis, Z.; Amara, K. K.; Pang, J. R.; Toh, M.; Zhang, X.; Kloc, C.; Tan, P. H.; Eda, G. Lattice Dynamics in Mono- and Few-Layer Sheets of WS_2 and WSe_2. *Nanoscale* **2013**, *5*, 9677–9683.
37. Dartigeas, K.; Gonbeau, D.; Pfister-Guillouzo, G. Core and Valence Spectra of TaS_2 and WS_2. Experimental and Theoretical Studies. *J. Mater. Chem. Faraday Trans.* **1996**, *92*, 4561–4566.
38. Wang, H.; Kong, D.; Johanes, P.; Cha, J. J.; Zheng, G.; Yan, K.; Liu, N.; Cui, Y. $MoSe_2$ and WSe_2 Nanofilms with Vertically Aligned Molecular Layers on Curved and Rough Surfaces. *Nano Lett.* **2013**, *13*, 3426–3433.
39. Gong, Y.; Liu, Z.; Lupini, A. R.; Shi, G.; Lin, J.; Najmaei, S.; Lin, Z.; Elías, A. L.; Berkdemir, A.; You, G.; *et al*. Band Gap Engineering and Layer-by-Layer Mapping of Selenium-Doped Molybdenum Disulfide. *Nano Lett.* **2013**, *14*, 442–449.
40. Xie, J.; Zhang, J.; Li, S.; Grote, F.; Zhang, X.; Zhang, H.; Wang, R.; Lei, Y.; Pan, B.; Xie, Y. Controllable Disorder Engineering in Oxygen-Incorporated MoS_2 Ultrathin Nanosheets for Efficient Hydrogen Evolution. *J. Am. Chem. Soc.* **2013**, *135*, 17881–17888.
41. Phuruangrat, A.; Ham, D. J.; Hong, S. J.; Thongtem, S.; Lee, J. S. Synthesis of Hexagonal WO_3 Nanowires by Microwave-Assisted Hydrothermal Method and Their Electrocatalytic Activities for Hydrogen Evolution Reaction. *J. Mater. Chem.* **2010**, *20*, 1683–1690.
42. Lin, J.; Peng, Z.; Wang, G.; Zakhidov, D.; Lario, E.; Yacaman, M. J.; Tour, J. M. Enhanced Electrocatalysis for Hydrogen Evolution Reaction from WS_2 Nanoribbons. *Adv. Energy Mater.* **2014**, *4*, 1301875−1–7.
43. Lukowski, M. A.; Daniel, A. S.; English, C. R.; Meng, F.; Forticaux, A.; Hamers, R. J.; Jin, S. Highly Active Hydrogen Evolution Catalysis from Metallic WS_2 Nanosheets. *Energy Environ. Sci.* **2014**, *7*, 2608–2613.
44. Merki, D.; Hu, X. Recent Developments of Molybdenum and Tungsten Sulfides as Hydrogen Evolution Catalysts. *Energy Environ. Sci.* **2011**, *4*, 3878–3888.
45. Wang, H.; Lu, Z.; Kong, D.; Sun, J.; Hymel, T. M.; Cui, Y. Electrochemical Tuning of MoS_2 Nanoparticles on Three-Dimensional Substrate for Efficient Hydrogen Evolution. *ACS Nano* **2014**, *8*, 4940–4947.